

Article

In Situ Trace Element and Sulfur Isotope Composition of Pyrite from the Beiwagou Pb-Zn Deposit, Liaodong Peninsula, Northeast China: Implications for Ore Genesis

Qi Yu ^{1,2}, Zhigao Wang ^{1,3,*}, Qingfei Sun ¹ and Keyong Wang ¹

¹ College of Earth Sciences, Jilin University, Changchun 130061, China

² Geological Survey Institute of Jilin Province, Changchun 130102, China

³ Northeast Geological S&T Innovation Center of China Geological Survey, Shenyang 110034, China

* Correspondence: wangzg19@jlu.edu.cn

Abstract: The Beiwagou Pb-Zn deposit, located in the western part of the Liaodong Peninsula, is a carbonate-hosted stratiform deposit with a Pb + Zn reserve of 0.08 Mt @ 4.14% (Pb + Zn). The orebodies occur as conformable layers and lenses and are strictly controlled by strata (the Paleoproterozoic Gaojiayu and Dashiqiao Formations) and lithology (plagioclase amphibolite and dolomitic marble). Given that previous studies have focused only on the mineralization features and mineralogy of deposits, herein, we report in situ trace element analyses of pyrite using LA-ICP-MS, together with in situ sulfur isotopes of pyrite, to constrain the composition, substitution mechanisms, source of sulfur, and sulfate reduction pathways of pyrite in the Beiwagou deposit. Based on pyrite morphology, texture, and chemistry, four pyrite types were identified: subhedral, porous-to-massive pyrite (Py1) related to chalcopyrite; subhedral, porous crushed pyrite (Py2) associated with fine-grained sphalerite; rounded and porous pyrite (Py3) related to the Zn-rich part of the laminated ore; and anhedral, porous-to-massive pyrite (Py4) associated with pyrrhotite, arsenopyrite, sphalerite, and galena. Py1 is characterized by high As, Ag, Cd, In, Au, Cu, and Zn concentrations and low Te, Bi, and Mo concentrations, whereas Py2 has high concentrations of Co and Ni and low concentrations of other trace elements, such as Cu, Zn, Bi, and Te. Py3 is characterized by elevated As concentrations, low Co, Ni, In, W, Te, and Tl concentrations, and varying Pb concentrations, whereas Py4 has low Ag, Cd, In, Zn, Cu, and Mn concentrations and varying W, Co, Ni, Pb, Sb, and As concentrations. Significant correlations between some elements in each pyrite type suggest substitution mechanisms, such as $(Zn^{2+} + Cu^{2+} + Mn^{2+} + Cd^{2+}) \leftrightarrow 2Fe^{2+}$, $Ag^+ + (Sb)^{3+} \leftrightarrow 2Fe^{2+}$, and $(Te^+ + Ag^+) + Sb^{3+} \leftrightarrow 2Fe^{2+}$, and the existence of a negative correlation between Co and Ni implies competition between both elements. The strongly positive $\delta^{34}S$ values (12.11‰–23.54‰) are similar to that of seawater sulfates and likely result from thermochemical sulfate reduction (TSR). In conclusion, the Beiwagou Pb-Zn deposit is a typical SEDEX deposit and mineralization likely occurred during diagenesis.



Citation: Yu, Q.; Wang, Z.; Sun, Q.; Wang, K. In Situ Trace Element and Sulfur Isotope Composition of Pyrite from the Beiwagou Pb-Zn Deposit, Liaodong Peninsula, Northeast China: Implications for Ore Genesis. *Minerals* **2023**, *13*, 1176. <https://doi.org/10.3390/min13091176>

Academic Editor: Maria Boni

Received: 26 July 2023

Revised: 29 August 2023

Accepted: 5 September 2023

Published: 7 September 2023



Copyright: © 2023 by the authors. Licensee MDPI, Basel, Switzerland. This article is an open access article distributed under the terms and conditions of the Creative Commons Attribution (CC BY) license (<https://creativecommons.org/licenses/by/4.0/>).

1. Introduction

The Liaodong Peninsula is located in the southern part of Liaoning Province in Northeast China and hosts numerous medium- and large-scale lead-zinc, gold, and silver deposits. These deposits can be divided into Paleoproterozoic strata-bound Pb-Zn mineralization (e.g., Zhenzigou, Dongsheng, and Beiwagou Pb-Zn deposits [1,2]) and Mesozoic magmatism-related vein-type Pb-Zn-Au-Ag mineralization (e.g., Baiyun and Wulong Au and Gaojiapuzi Ag deposits [3–5]). Previous studies have shown that later magmatism-related Pb-Zn veins were spatially superimposed onto the former stratiform Pb-Zn orebodies (e.g., the Zhenzigou Pb-Zn deposit [2,6]), which is also documented in many ore districts worldwide, e.g., the Yenefrito Pb-Zn mine in the Pyrenees, Spain [7],

the Macmillan Pass Pb-Zn ± Ba deposit in Yukon, Canada [8], and the Red Dog Zn-Pb-Ag district, Northern Alaska [9]. Due to essential base metal elements, studies on the mineralization process of lead-zinc deposits have been pursued by scholars around the globe, and the type of genesis can be classified into SEDEX [2], skarn [10,11], Mississippi Valley-type (MVT) [12], and hydrothermal vein-type deposits [13]. In this context, the ore genesis and metal sources of the Pb-Zn deposits in the Liaodong Peninsula are still debated, as indicated by the Proterozoic seafloor exhalation model [2,14] and the sedimentation metamorphism-hydrothermal reworking model [15,16]. In addition, hypotheses about these strata-bound sedimentary-dominated Pb-Zn deposits formed by either true exhalative processes or subseafloor replacement during sedimentation or early diagenesis are contentious [17–19].

As a ubiquitous mineral in various ore systems, pyrite incorporates numerous trace elements (e.g., Ag, As, Au, Bi, Co, Cu, Mn, Mo, Ni, Pb, Sb, Se, Tl, and Zn), which are either substituted within the crystal lattice or exist as nanoparticles or micro-inclusions [20,21]. Previous studies have shown that variations in pyrite textures and compositions can reflect changes in the fluid signatures and/or precipitation conditions during the evolution of the hydrothermal system [22–24]. For instance, pyrite has a homogeneous distribution of trace elements in sub-seafloor replacement processes but this is not the case in exhalation processes that involve a significant loss of metals through dispersion on the seafloor [25,26]. Detailed pyrite studies (e.g., those implementing laser ablation inductively coupled plasma mass spectrometry (LA-ICP-MS)) can detect these subtle variations during ore precipitation and have been commonly applied to porphyry [23], skarn [27], VMS [28,29], and SEDEX [19,30] deposits.

Previous sulfur isotope analyses of sulfide separates have some obvious limitations, especially when considering fine-grained sulfide minerals (e.g., pyrite) with complex textures and multiple sources in superimposing deposits. In situ sulfur isotope analysis using high-spatial-resolution ion microprobe instruments (e.g., those used in secondary ion mass spectrometry (SIMS)) can measure the variability in the sulfur isotope composition of fine-grained intergrown sulfide minerals [31,32]. This method is useful for distinguishing between syngenetic, diagenetic, and epigenetic pyrite in strata-bound sedimentary-dominated Pb-Zn deposits [33,34].

The Beiwagou deposit, a typical strata-bound Pb-Zn deposit in the Liaodong Peninsula, was formed in the Paleoproterozoic Gaojiayu and Dashiqiao Formations and has a Pb + Zn reserve of 0.08 Mt @ 4.14% (Pb + Zn) [35]. Previous studies have focused only on the mineralization features [35] and mineralogy [36] of deposits. The Beiwagou Pb-Zn deposit was proposed to be a sedimentary metamorphic deposit that was modified by later hydrothermal fluids [35]. Nevertheless, there is no convincing evidence on the mineralization process. Here, we present detailed in situ pyrite trace element and sulfur isotope composition measurements that can provide critical information about the pyrite's growth history and conditions and processes of ore formation and can distinguish origins. These results are useful for investigating the relationship between pyrite formation and base metal sulfide mineralization as well as for developing a robust deposit model for the formation of the Beiwagou deposit.

2. Geological Setting

The Liaodong Peninsula (the Liaodong Rift Zone, ca. 700 km in the NNE) is bordered by the Tanlu fault in the west and the Japan Sea in the east and records the main geological evolution of the North China Craton (NCC) from the Archean to the Cenozoic (Figure 1). Regionally exposed strata comprise (i) the Archean metamorphic Anshan Group, comprising mainly amphibolite, magnetite quartzite, plagiogneiss, and granulite [37], and (ii) the Paleoproterozoic metamorphic Liaohe Group (including Langzishan, Lieryu, Gaojiayu, Dashiqiao, and Gaixian Formations) comprising a suite of greenschist-epidote-amphibolite-facies metamorphosed clastic and volcano-sedimentary rocks [38], and (iii) Paleozoic-to-Mesozoic clastic and volcanic sequences, for example, Cambrian,

Ordovician, Carboniferous, and Permian-to-Cretaceous rocks [39]. The Anshan Group, a product of the recycling of ancient crustal material, is an Anshan-type BIF iron-ore host that includes the Waitoushan, Qidashan, Xi'anshan, Baoguolao, Xiaolaihe, and Yanglin iron deposits [37,40]. The Liaohe Group hosts strata-bound sedimentary-dominated deposits (including Pb-Zn, Cu-Co, boron, talc, and magnesite deposits) such as the Zhenzigou Pb-Zn [2], Dahenglu Cu-Co [41], Houxianyu boron [42], Yangjiadian talc [43], and Qingshanhui magnesite [44] deposits. The protoliths of the metavolcanic rocks from the Liaohe Group were formed at ca. 2.19 Ga and were modified by a metamorphic event around 1.90 Ga. The evolutionary mechanism may be related to arc-continent collision [38,45]. These Paleoproterozoic strata and deposits are partly hosted in the core and limbs of the NWW/NEE-trending anticlines/synclines (e.g., Dashiqiao-Caohekou, Hupiyu-Kuandian, and Gaixian-Xiuyan). Paleozoic-to-Mesozoic volcano-sedimentary units are generally bounded by regional EW/NE-trending faults and their secondary structures (e.g., Fuzhou-Daziying, Yalvjiang, and Xiongyue-Anshan).

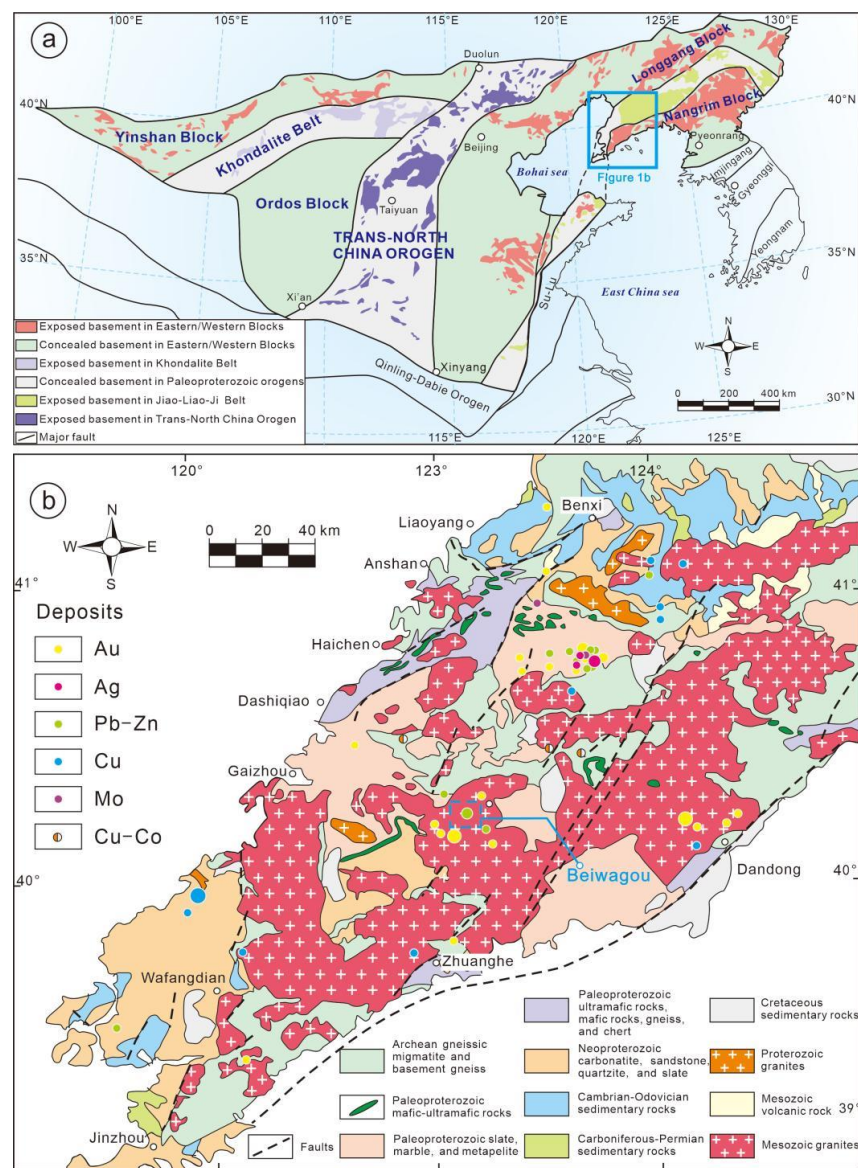


Figure 1. (a) Geologic map of the NCC (after [46]). (b) Geological map of the Liaodong Peninsula (after [3]).

Magmatism in the Liaodong Peninsula occurred during four episodes: (1) the Paleoproterozoic (ca. 2332–1756 Ma), (2) the Triassic (ca. 243–210 Ma), (3) the Jurassic (ca. 196–144 Ma), and (4) the Early Cretaceous (ca. 130–120 Ma) [2]. The Paleoproterozoic intrusive rocks comprise mainly gneissic granite, monzogranite, syenogranite, and granitic pegmatite [45,47], and their formation ages are concentrated at approximately 2332–2132 Ma and 1904–1756 Ma, respectively, which are related to collisions and extensions of the Liaonan block to the south and the Longgang block to the north [1,43,45]. Magmatism corresponds to three major orogenic/mobile belts during Mesozoic, namely the Central Asian orogenic belt on its northern margin, the Dabie–Sulu orogenic belt on its southern segment, and the subduction of the Pacific Plate on its eastern margin [2]. The Mesozoic plutons, including monzogranite, granodiorite, biotite granite, quartz diorite, etc. [39,47–51], show a close spatial-temporal-genetic link with the Au-Ag and local vein-type Pb-Zn mineralization (e.g., the Wulong Au, Baiyun Au, and Gaojiapuzi Ag deposits and the Xinling Ag-Pb-Zn deposits [2,52,53]).

3. Ore Deposit Geology

The Beiwagou Pb-Zn deposit ($40^{\circ}27'02''$ N, $123^{\circ}02'08''$ E) is located in the western part of the Liaodong Peninsula (Figure 1b). Local strata mainly include the Gaojiayu and Dashiqiao Formations of the Paleoproterozoic Liaohe Group and Quaternary sediments (Figure 2). The Gaojiayu Formation (strike: $290\text{--}310^{\circ}$, NE dipping at $50\text{--}60^{\circ}$) is mainly distributed in the northern part of the ore district and is comprised of plagioclase hornblende, graphite-bearing marble, and biotite-tremolite-graphite granulite. The Dashiqiao Formation, the chief ore-bearing strata in the ore district, conformably overlies the Gaojiayu Formation and is distributed in the central part of the ore district. It can be divided into three units (e.g., D₁, D₂, and D₃) based on different lithological assemblages. Unit D₁ consists primarily of graphite-bearing marble, whereas unit D₂ comprises garnet/sillimanite-mica schist and dolomitic marble. Unit D₃ contains banded dolomitic and tremolite-bearing marble. Local structures include mainly NW/NE-trending faults and secondary EW-trending faults (Figure 2) and were formed after lead-zinc mineralization, which cut some stratiform orebodies but were limited in scale. Magmatic rocks are mainly discovered in the northern and southern parts of the ore district (Figure 2) and belong to the Paleoproterozoic Liaoji granite that was intruded upon by late Mesozoic magmatism (ca. 157.4–156.3 Ma [54]).

The orebodies of the Beiwagou deposit occur as conformable layers and lenses and are strictly controlled by strata (Paleoproterozoic Gaojiayu and Dashiqiao Formations) and lithology (plagioclase amphibolite and dolomitic marble) (Figure 3). Twelve NW-trending Pb-Zn orebodies (e.g., No. I, I-1, II, III, III-1, and V) have been delineated in the ore district, striking at $280\text{--}310^{\circ}$ and dipping $35\text{--}60^{\circ}$ NE. These orebodies are 46–305 m long and 0.61–13.03 m thick, with ore grades of 0.3%–0.79% Pb and 2.58%–9.74% Zn. Beiwagou Pb-Zn mineralization occurs mostly as layers, lenses, and veins and minorly as breccias and dissemination (Figure 4). The late Mesozoic intrusive bodies or dikes and vein-type Pb-Zn mineralization are significantly governed by the EW-trending and NW-trending faults, implying a close connection among them. The scales of vein-type orebodies are finite despite the grades achieving industrial requirements. The ore minerals of the Beiwagou Pb-Zn deposit are predominantly sphalerite, galena, and pyrite, along with minor chalcopyrite, arsenopyrite, marcasite, and pyrrhotite (Figure 5). The gangue minerals include dolomite, tremolite, diopside, talc, taxonite, and quartz. Wallrock alterations are predominantly serpentinization, dolomitization, and silicification, which are closely related to Pb-Zn mineralization.

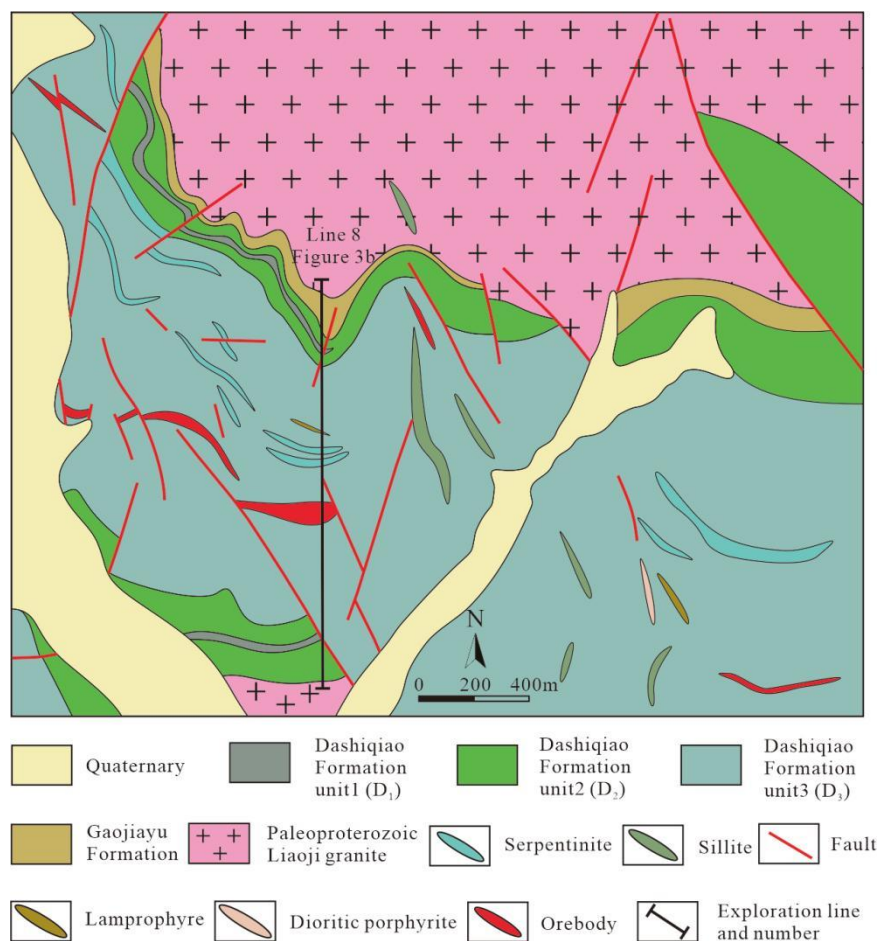


Figure 2. Geologic map of the Beiwigou Pb-Zn deposit (modified from [35]).

The delicately laminated nature of the Pb-Zn mineralization at Beiwigou and the surrounding carbonaceous host rocks (e.g., dolomitic marble) of the Gaojiayu and Dashiqiao Formations indicate that deposition occurred in a relatively static tectonic setting (Figures 3 and 4). Localized laminated orebodies show soft-sediment deformation features, such as slumping, folding, and dewatering pipes (Figure 4c,d). These soft-sediment deformation features may be related to the late Paleoproterozoic compressional tectonism (e.g., ca. 1800 Ma, during the “Lvliang Movement”) [53,55,56].

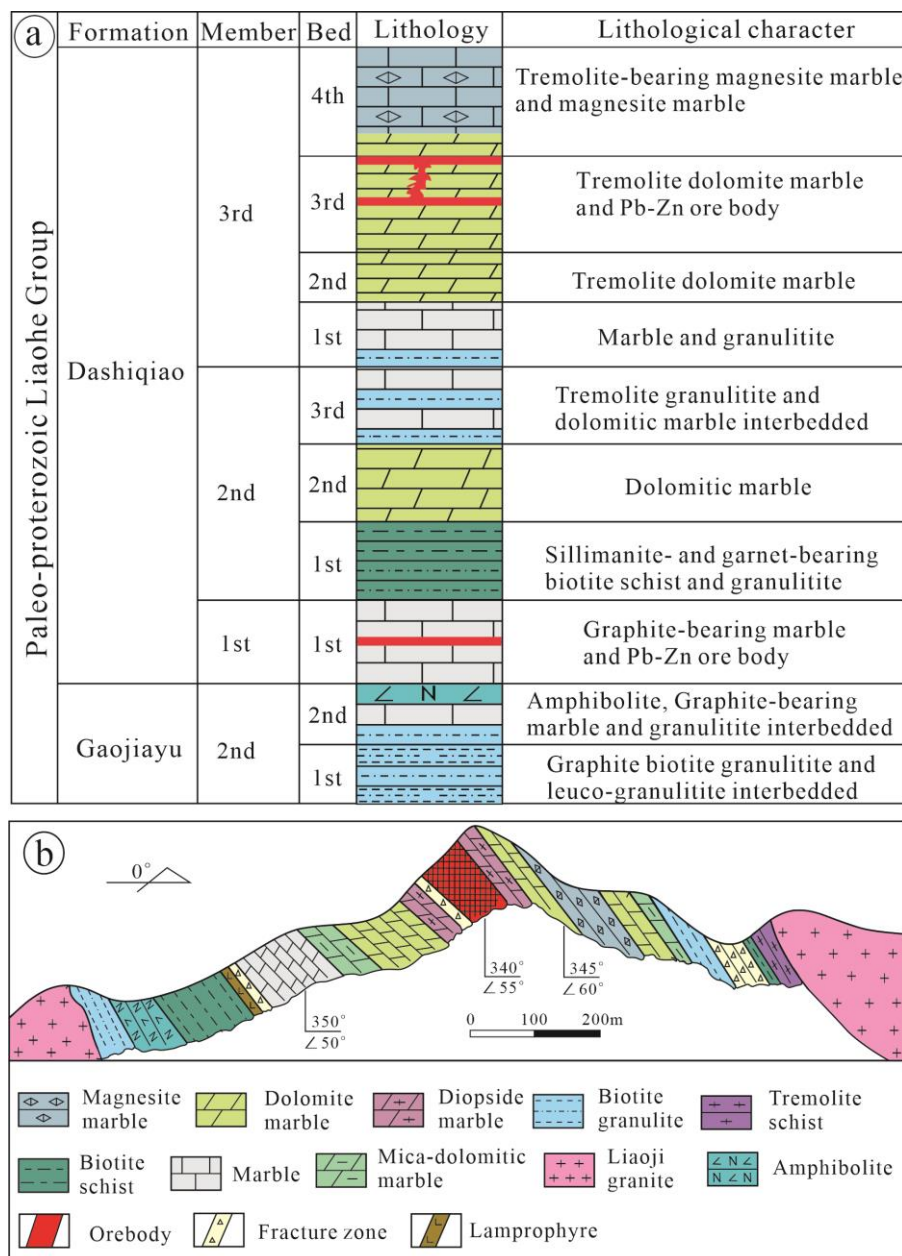


Figure 3. (a) Stratigraphic column of the Beiwagou Pb-Zn deposit; (b) The No. 8 exploration section map in the Beiwagou Pb-Zn deposit (modified from [35]).

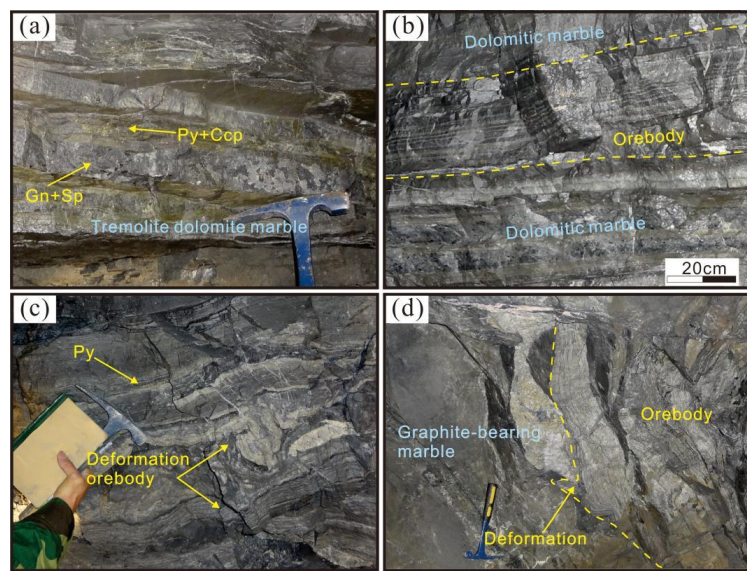


Figure 4. Photographs of strata-bound mineralization in tremolite dolomite marble (a) and dolomitic marble (b) of the Dashiqiao Formation; (c,d) Deformation orebodies in the Beiwagou deposit.

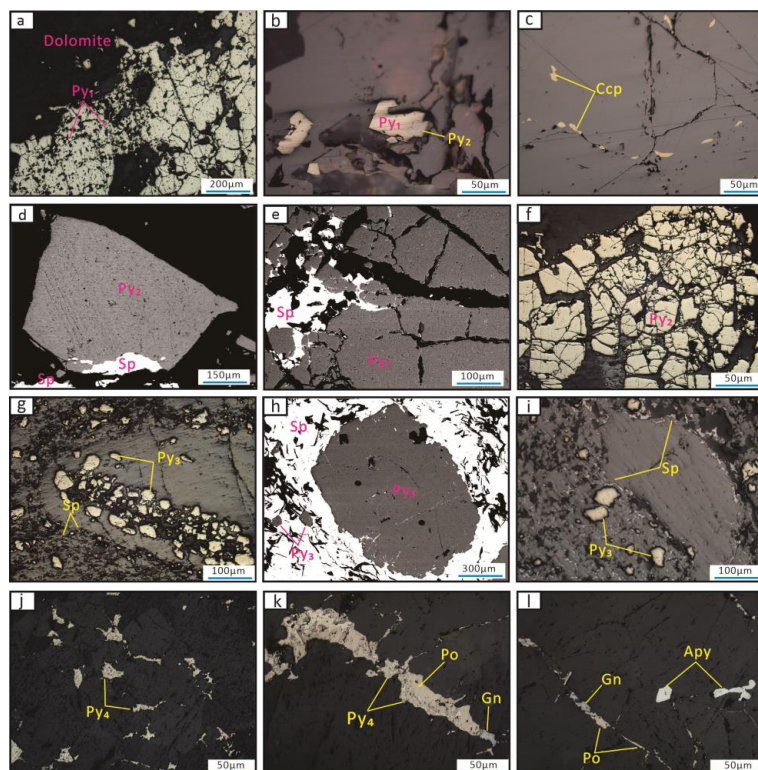


Figure 5. Photomicrographs of the Beiwagou Pb-Zn ore textures: (a) Subhedral, porous-to-massive pyrite (Py1); (b) Subhedral, porous-to-massive pyrite (Py1) and subhedral, porous crushed pyrite (Py2) developed in dolomitic marble; (c) Fine-grain chalcopyrite in the Py1; (d,e) Py2 replaced with sphalerite (BSE image); (f) Subhedral, porous crushed pyrite (Py2); (g) Clusters of rounded and porous pyrite (Py3); (h) Py3 replaced with sphalerite (BSE image); (i) Py3 replaced with sphalerite; (j) Anhedral, porous-to-massive pyrite (Py4); (k) Py4 replaced with pyrrhotite and galena; (l) Py4 replaced with pyrrhotite, galena, and arsenopyrite. Abbreviations: Apy = Arsenopyrite; Ccp = Chalcopyrite; Gn = Galena; Po = Pyrrhotite; Py = Pyrite; Sp = Sphalerite.

4. Sampling and Analytical Methods

4.1. Sampling Strategy

The samples were collected from underground mine working sites (e.g., PD3, 5, and 330) and drill cores (e.g., ZK8604, ZK8605, ZK8611, and ZK9006) from the Beiwagou deposit. Based on microscopic observations under transmitted and reflected light, a representative suite of samples were selected for trace element and sulfur isotopic analyses.

4.2. In Situ LA-ICP-MS Analyses

In situ LA-ICP-MS analyses were performed using an Analytik Jena PlasmaQuant MS Elite ICP-MS with a RESolution SE 193 nm excimer laser denudation system at Beijing Createch Testing Technology Co., Ltd. (Beijing, China) [57]. Quantitative pyrite analyses were conducted by ablating a series of trenches in a high-purity He atmosphere to minimize beam attenuation and obtain an even ablation profile. The laser denudation was performed with a beam diameter of 30 μm , a laser frequency of 6 Hz, and an energy density of about 6 J/cm^2 . The analysis time for each sample was 85 s, including a 40 s background with the laser off and 45 s analysis with the laser on. External standards, including synthetic glass standards NIST 611 and 612, as well as MASS-3, BHVO-2G, BCR-2G, and BIR-1G, were used at intervals of one every 10 denudation points for quantitative analyses [58]. Sample and blank signal selection, instrument sensitivity drift correction, and elemental content calculation were performed using ICPMSData Cal (v7.8) software.

4.3. In Situ Sulfur Isotope Analyses

In situ sulfur isotope analysis was performed on the same samples analyzed via LA-ICP-MS at Beijing Createch Testing Technology Co., Ltd (Beijing, China). The analysis was performed using a RESolution SE 193 nm LA system coupled with a Neptune Plus Multi-Collector (MC)-ICP-MS. Pyrite and reference material samples were analyzed using 20 to 30 μm spot sizes at a frequency of 5 Hz with an energy density of 3 J/cm^2 . High-purity helium was used as a carrier gas at a flow rate of 320 mL/min. ^{32}S and ^{34}S were statically received simultaneously with a Faraday cup detector array, and the integration time was 0.131 s. Each analysis took approximately 27 s to collect 200 sets of data. Standard WS-1 was utilized as external standard for sulfur isotope fractionation correction. Results are reported as $\delta^{34}\text{S}$ relative to Vienna Canyon Diablo Troilite (V-CDT) with a precision of $\pm 0.2\text{\textperthousand}$.

5. Results

5.1. Pyrite Types

Based on pyrite morphology, texture, and chemistry, four pyrite types were identified in the Beiwagou Pb-Zn deposit, including subhedral, porous-to-massive pyrite (Py1) (Figure 5a–c), subhedral, porous crushed pyrite (Py2) (Figure 5d–f), rounded and porous pyrite (Py3) (Figure 5g–i), and anhedral, porous-to-massive pyrite (Py4) (Figure 5j–l). In accordance with the formation sequence of the minerals and the associations of pyrite with the mineral assemblages, the four pyrite species were generated in the order of formation from Py1 to Py4. The detailed characteristics of each type of pyrite are described below.

Py1 was composed of subhedral-to-euhedral pyrite related to the Cu-rich part of the ore. The pyrite crystallites had a narrow range of diameters (40–100 μm , 65 μm on average) and locally occurred with chalcopyrite, commonly <10 μm in diameter.

Py2 was identified by its subhedral and crushed crystals, probably due to deformation from late Paleoproterozoic compressional tectonism. The grains were generally coarser (100–1100 μm , average of 400 μm) than in any other part of the deposit and locally filled with sphalerite (<10 μm) in the fracture space.

Py3 consisted of irregular and rounded pyrite crystallites related to the Zn-rich part of the laminated ore. These pyrite layers followed the bedding in the dolomitic marble independently or in groups. The grains had a wide range of diameters (<10–800 μm , 40 μm on average) and occurred with sphalerite crystallites, commonly 5 to 20 μm in diameter.

Py4 was defined by its association with pyrrhotite, arsenopyrite, sphalerite, and galena. Numerous macroscopic and petrographic observations have shown that pyrrhotite and sphalerite locally replace anhedral pyrite. The pyrite crystallites also had a wide range of diameters (20–500 μm , with an average of 150 μm).

5.2. Trace Element Characteristics of Pyrite

Seventeen trace elements were measured in all the pyrite varieties by LA-ICP-MS analysis (Table S1). Elements such as Mn, As, Co, Ni, Cu, Cd, Zn, In, W, Te, and Au show distinct trace element characteristics for each of the four pyrite types, as illustrated in Figure 6.

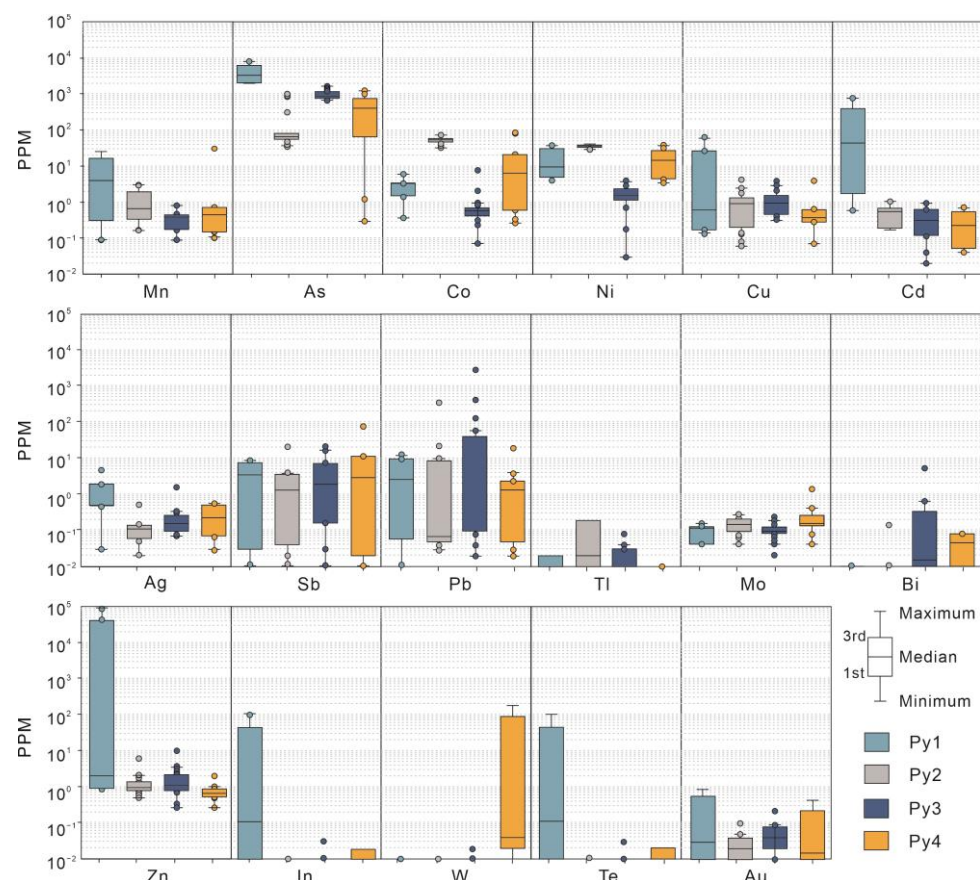


Figure 6. Simple box and whisker plots of trace element contents of each pyrite type (including Py1, Py2, Py3, Py4).

Py1: The trace element composition of the pyrite-chalcopyrite assemblage (Py1) is distinct in that it is characterized by elevated As (1980.75–8044.62 ppm), Ag (0.03–4.75 ppm), Cd (0.59–776.26 ppm), In (0.01–109.93 ppm), Au (0.01–0.88 ppm), Cu (0.14–59.60 ppm), and Zn (0.88–93,853.23 ppm) and low Te (<0.54 ppm), Bi (<0.01 ppm), and Mo (0.03–0.15 ppm) concentrations (Figure 6; Table S1). The data for Py1 formed the largest cluster in the box and whisker plots of trace element content when compared to the other pyrite types (Figure 6). The enriched Zn concentrations of Py1 were scattered within single grains and showed a strong association with Cd, In, Cu, Ag, and Mn and a minor association with Sb and Pb (Figure 7A).

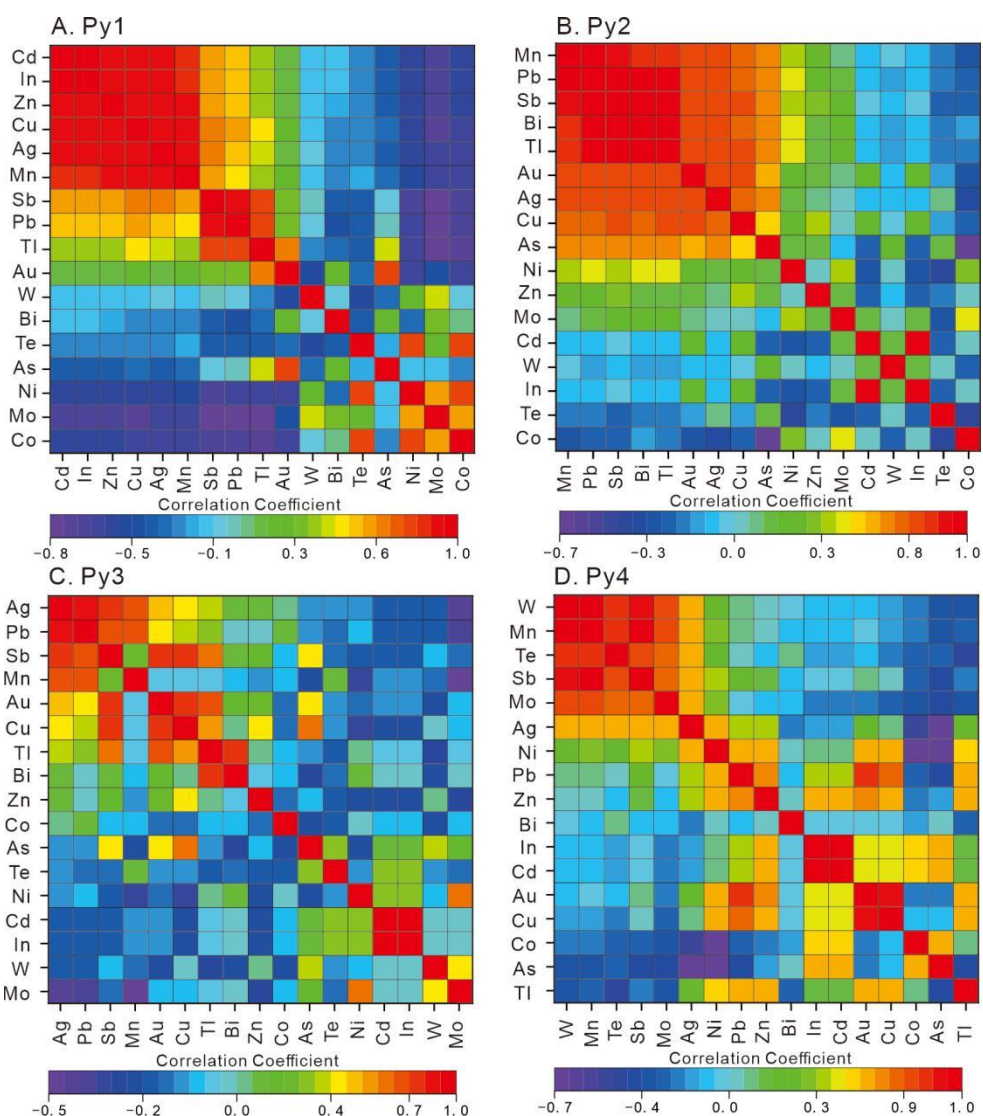


Figure 7. Correlation matrices showing element compositions of each pyrite type (including Py1, Py2, Py3, Py4).

Py2: Eighteen spots in four samples containing recrystallized and overgrown pyrite were analyzed. Py2 has higher Co (31.90–72.27 ppm) and Ni (29.52–41.14 ppm) concentrations than the other pyrite types (average = 1.64 ppm (Py3), 15.12 ppm (Py4), and 13.92 ppm (Py1)) (Figure 6; Table S1). But contents of some trace elements are low in Py2 grains, such as Cu (0.06–4.21 ppm), Zn (0.49–6.03 ppm), Bi (0.01–0.14 ppm), and Te (0.11–0.17 ppm). For Py2, positive correlations were observed between Pb and elements including Mn, Sb, Bi, Tl, Au, Ag, Cu, and As, together with the In vs. Cd correlation (Figure 7B).

Py3: Seventeen spots in three samples were observed on the rounded and porous pyrite. The result indicates very little chemical spread that is characterized by elevated As (665.86–1647.51 ppm), low Co (0.07–7.58 ppm), Ni (0.03–3.76 ppm), In (0.01–0.03 ppm), W (0.01–0.02 ppm), Te (0.01–0.89 ppm), and Tl (0.01–0.08 ppm), and varying Pb (0.02–2955.15 ppm) concentrations (Figure 6; Table S1). The scatter of Pb concentrations may be due to small inclusions in the porous pyrite. Positive correlations were observed between Pb and Ag, Sb, Mn, and Au, together with Au and Cu, Au and Tl, Au and Sb, In and Cd, and Bi and Tl (Figure 7C).

Py4: Chemically, the pyrite related to the pyrite-pyrrhotite-arsenopyrite assemblage (Py4) is clearly identified by low Ag (0.03–0.56 ppm), Cd (0.04–0.69 ppm), In (0.01–0.02 ppm), Zn (0.26–1.98 ppm), Cu (0.07–3.92 ppm), and Mn (0.11–25.45 ppm) and varying W (0.03–

180.75 ppm), Co (0.26–83.87 ppm), Ni (3.47–37.53 ppm), Pb (0.02–19.88 ppm), Sb (0.01–73.94 ppm), and As (0.29–1223.66 ppm) concentrations (Figure 6; Table S1). Py4 displays a broad positive correlation between W and elements such as Mn, Te, Sb, and Mo, together with Au vs. Cu and Cd vs. In (Figure 7D).

5.3. Sulfur Isotope Compositions

The sulfur isotope compositions of Py1, Py2, Py3, and Py4 had slightly narrow and highly positive ranges of $\delta^{34}\text{S}$ values (Table 1; Figure 8). The sulfide $\delta^{34}\text{S}_{\text{V}-\text{CDT}}$ values are 12.11‰–12.33‰ (mean: 12.23‰; Py1), 18.01‰–18.50‰ (mean: 18.25‰; Py2), 16.66‰–23.54‰ (mean: 18.89‰; Py3), and 14.24‰–15.00‰ (mean: 14.62‰; Py4).

Table 1. LA-MC-ICP-MS in situ S isotope compositions of each pyrite type from the Beiwagou Pb-Zn deposit.

Sample No.	$\delta^{34}\text{S}_{\text{V}-\text{CDT}} (\text{\textperthousand})$	Generations
BWG-4-1	12.33	Py1
BWG-4-2	12.11	Py1
BWG-4-3	12.25	Py1
BWG-4-4	18.01	Py2
BWG-7-1	18.23	Py2
BWG-7-2	18.50	Py2
BWG-3-1	14.24	Py4
BWG-3-2	15.00	Py4
BWG-6-1	16.66	Py3
BWG-6-2	17.38	Py3
BWG-6-3	19.65	Py3
BWG-6-4	23.54	Py3
BWG-6-5	17.24	Py3

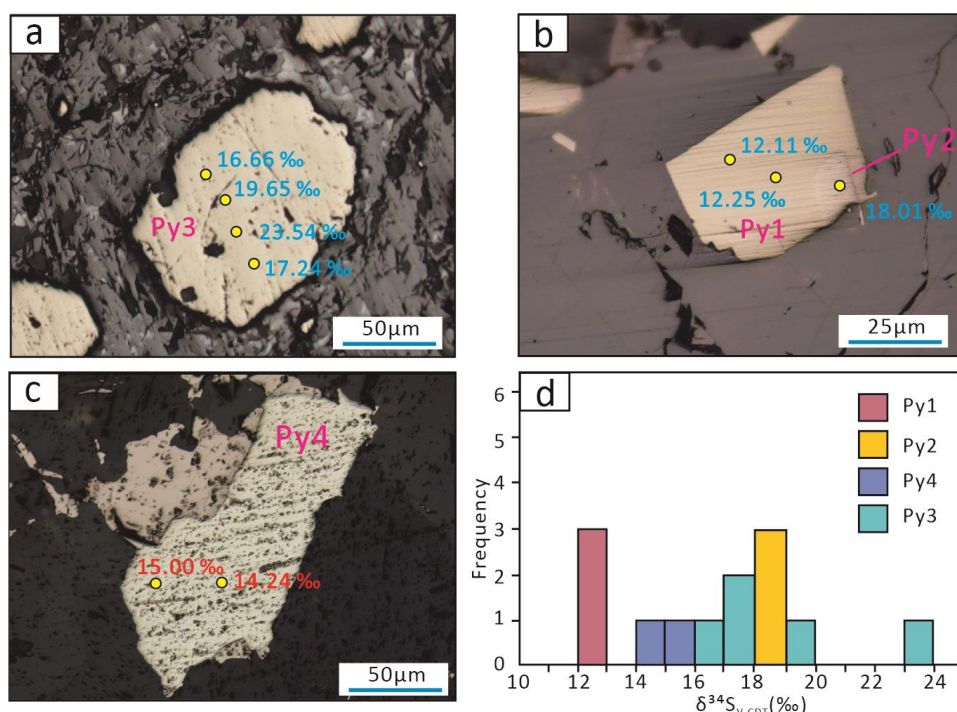


Figure 8. $\delta^{34}\text{S}$ values of representative pyrites: (a–c) Positive $\delta^{34}\text{S}$ values (TSR signature) in each pyrite type (including Py1, Py2, Py3, Py4); (d) Sulfur isotopic composition of pyrites in Beiwagou deposit.

6. Discussion

6.1. Partitioning of Trace Elements

Previous studies have demonstrated that many elements (e.g., Ag, Co, Ni, Sn, Zn, Au, Cu, As, Bi, Mn, Te, and Mo) have similar ionic radii to that of Fe^{2+} and are easily incorporated into the pyrite lattice via isomorphous substitution [59,60]. Huston et al. [20] suggested that these elements occur as either nonstoichiometric lattice substitutions (e.g., Cu, Mo, and Bi) or stoichiometric lattice substitutions (e.g., Co and Ni) within pyrite crystals. Therefore, the preferential concentration in pyrite can record not only changes in the physicochemical parameters of the parental fluid but also the subsequent deformation, dissolution-remobilization, and recrystallization processes.

The box and whisker plots of the trace element contents show that Py3 is more depleted in Co and Ni than Py4, Py1, and Py2 (Figure 6). This suggests that the fluids are barren in Co and Ni in nature or that little Co and Ni are partitioned to the pyrite via the isomorphous replacement of Fe. In addition, average Co and Ni ratios (1.38) are commonly accepted to indicate pyrite of sedimentary origin, as pyrite related to hydrothermal fluids has Co/Ni ratios of $>>1$ [61,62]. The abundance of As in all pyrite types may be associated with the significant substitution of As for S in the pyrite lattice. The Cd and In contents of all pyrite types showed a positive correlation (Figure 7), indicating that Cd and In entered the pyrite lattice via isomorphism. The low Mo content in the Beiwagou pyrite (up to 1.35 ppm) may reflect widespread oxidizing seawater conditions [63].

Py1 has higher Mn, Cd, As, In, and Te contents than other pyrite types, which is likely caused by surface defects in the pyrite lattice that facilitate elemental residence [64]. Metals with ionic sizes close to that of Fe^{2+} , such as Zn^{2+} , Cu^{2+} , Mn^{2+} , and Cd^{2+} , are generally incorporated into pyrite structures in the form $(\text{Zn}^{2+} + \text{Cu}^{2+} + \text{Mn}^{2+} + \text{Cd}^{2+}) \leftrightarrow 2\text{Fe}^{2+}$. The median values of As, Cd, In, and Te in Py1 were higher than those in the other pyrite types (Figure 6), indicating that the bulk replacement of S by As can promote a higher uptake of Cd, In, and Te in a more reduced environment. Py2 has higher Co (31.90–72.27 ppm) and Ni (29.52–41.14 ppm) concentrations than the other pyrite types (average = 13.92 ppm (Py1), 1.64 ppm (Py3), and 15.12 ppm (Py4)) (Figure 6; Table S1). However, a low correlation between Co and Ni was observed for each pyrite type, suggesting that Co and Ni are not direct substitutes for Fe in the pyrite lattice, forming Co- and Ni-bearing sulfides such as Co-pentlandite and pentlandite $((\text{Fe}, \text{Ni})_9\text{S}_8)$. In addition, Sb shows positive correlations with Pb, Cu, and As in Py2 (Figure 7), which likely implies that some Sb may present in the pyrite lattice in the form of tetrahedrite $((\text{Cu}, \text{Fe})_{12}\text{Sb}_4\text{S}_{13})$ and freieslebenite (AgPbSb_3) inclusions and behaves similarly to As when incorporated into the pyrite structure. The high correlation of the Ag, Pb, and Sb contents in Py3 suggests that Sb is incorporated into pyrite as a trivalent cation through the coupled substitution of $\text{Ag}^+ + (\text{Sb})^{3+} \leftrightarrow 2\text{Fe}^{2+}$. However, due to its large ionic size, Pb barely enters the pyrite lattice. Most Pb occurs as a solid solution in pyrite and as a minor direct substitution of $\text{Fe}^{2+} \leftrightarrow \text{Pb}^{2+}$ in the pyrite structure [65]. Py4 and Py1 mostly have Co/Ni ratios < 1 , which indicates that Co^{2+} and Ni^{2+} directly substitute for Fe^{2+} in pyrite [66,67]. The strong correlation between W, Mn, and Mo in Py4 may be attributed to the incorporation of them into the pyrite structure via the simple substitution equation: $\text{M}^{2+} \leftrightarrow \text{Fe}^{2+}$, while the strong correlation between monovalent and trivalent cations, such as Te, Ag, and Sb, may likely be caused by coupled substitutions in the pyrite lattice: $(\text{Te}^+ + \text{Ag}^+) + \text{Sb}^{3+} \leftrightarrow 2\text{Fe}^{2+}$.

6.2. Source of Sulfur

The $\delta^{34}\text{S}$ values for each pyrite type are strongly positive (12.11‰–23.54‰; Figure 8; Table 1) and similar to those of seawater sulfates (20‰ [68]), which is the predominant source of sulfur in stratiform, sediment-hosted Zn-Pb polymetallic deposits in most cases (e.g., [34,69]). Owing to the interference of the physicochemical properties of the ore fluid, such as the oxygen fugacity (f_{O_2}), temperature, pH, and ionic strength [70], the sulfur isotopic composition ($\delta^{34}\text{S}_i$) of sulfides generally does not represent the sulfur content ($\delta^{34}\text{S}_{\Sigma\text{S}}$) of the ore fluids. In order to reliably estimate the sulfur content of the ore fluids

from the pyrite data, it is necessary to know the temperature at which the pyrite was deposited. However, we could not obtain the formation temperature of the Beiwagou deposit because of a lack of microthermometric data for fluid inclusions and geothermal data for suitable mineral pairs. In most cases, the SEDEX-type Pb-Zn deposits were formed in a medium-low-temperature environment (e.g., 150–270 °C [71]). For this temperature range, the $\delta^{34}\text{S}$ value of pyrite corresponding to that of H₂S is 2‰ at 150 °C and 1‰ at 270 °C. Thus, we calculated that the $\delta^{34}\text{S}$ value of H₂S in the ore-forming fluid was 21‰–22‰ of the maximum $\delta^{34}\text{S}$ value analyzed for pyrite (~23‰) at Beiwagou and the above fractionation between pyrite and H₂S. Obviously, this is consistent with the $\delta^{34}\text{S}$ value of seawater for the Paleoproterozoic (~20‰ [72–74]). Therefore, we believe that the sulfur in the Beiwagou Pb-Zn deposit was sourced from coeval seawater sulfate.

6.3. Sulfate Reduction Pathways

There are several possible mechanisms for generating reduced sulfur (e.g., bacterial sulfate reduction (BSR) and thermochemical sulfate reduction (TSR)); the pathways by which sulfate is reduced to sulfide are still debated and remain contentious. BSR leads to the reduction of sulfate through bacterial respiration in an anaerobic environment, triggering a reaction of $2\text{CH}_2\text{O} + \text{SO}_4^{2-} \rightarrow 2\text{HCO}_3^- + \text{H}_2\text{S}$ [75]. TSR, which is an abiogenic process, reduces sulfate to sulfide by oxidizing labile organic carbon during diagenesis [76]. Although these two sulfate reduction pathways occur in different environments and processes, the end products of BSR and TSR are similar. Machel [75] suggested that the sulfur isotope composition of sulfide minerals could be effectively used to distinguish these processes. The presence of non-framboidal pyrite and high positive $\delta^{34}\text{S}$ values for each pyrite type from the Beiwagou deposit imply that the contribution of BSR sulfur to stratiform sediment-hosted Zn-Pb mineralization is not significant. This is because BSR can shrink the sulfate reservoir and subsequently increase the $\delta^{34}\text{S}$ value of sulfide as a sulfate-limited closed system in the ambient water column, which requires lower temperatures (<100 °C) to sustain microbial life [77]. BSR commonly leads to very negative $\delta^{34}\text{S}$ values and synsedimentary framboidal pyrite, which are shown in some SEDEX-type deposits elsewhere, such as the Howard's Pass SEDEX-type Zn-Pb deposit, Canada (−26 to −4.6‰ [33]), the Dajiangping pyrite deposit, China (−30 to −16‰ [34]), and the Navan Zn-Pb deposit, Ireland (−25 to −5‰ [78]).

As an important role in the formation of either vent-proximal or vent-distal SEDEX deposits, TSR by hydrothermal fluids generally occurs in higher-temperature environments (>100–140 °C) and significantly increase the $\delta^{34}\text{S}$ value of sulfide (TSR of seawater: 18‰–19‰ [79]). This is consistent with the highly positive $\delta^{34}\text{S}$ value of each pyrite type at Beiwagou from 12.11 to 23.54‰. Previous studies have experimentally determined that the kinetic fractionation between parent sulfate and daughter sulfide, expressed as $\Delta^{34}\text{S}_{\text{SO}_4-\text{H}_2\text{S}}$, is 20, 15, and 10‰ at 100, 150, and 200°C, respectively [80]. Assuming that the initial $\delta^{34}\text{S}$ sulfate value was approximately 30‰, the $\delta^{34}\text{S}$ values (12.11‰–23.54‰) of each pyrite type at Beiwagou are consistent with TSR at 150 to 200 °C ($\Delta^{34}\text{S}_{\text{SO}_4-\text{H}_2\text{S}} = 10\text{‰}–15\text{‰}$). The temperature at which TSR occurs is consistent with the formation temperature of the SEDEX-type Pb-Zn deposit mentioned above.

6.4. Integrated Model for the Genesis of the Beiwagou Deposit

The stratiform nature of the orebodies and sulfide lamination are essential features of the Beiwagou deposit and are generally considered evidence of the SEDEX origin of deposits of this type (e.g., [19,34,81]). Recent studies on the genesis of stratiform sediment-hosted Pb-Zn deposits have shown that the diagenetic model is superior to the original synsedimentary-exhalative model. For instance, Gadd et al. [33] concluded that most of the mineralizing events in the Howard's Pass SEDEX Zn-Pb district took place in the pores of sediments during diagenesis, as is also the case for the HYC Zn-Pb-Ag and Tom-Jason Pb-Zn-Ba deposits [82,83]. Pyrite is a moderately refractory mineral that can retain its texture and trace composition during low-grade metamorphism but undergoes extensive

recrystallization and trace composition changes in the presence of hydrothermal fluids [84]. Therefore, the texture and compositional changes of pyrite in different generations can effectively reflect the genesis of stratiform sediment-hosted Pb-Zn mineralization in Beiwagou.

As mentioned above, much of the Py3 in the stratified ores of the Beiwagou deposit occurs as rounded and anhedral crystals with a wide range of diameters (<10–800 μm , 40 μm on average), suggesting the replacement of the dolomitic marble during diagenesis. This is an important process in the formation of laminated sulfide ores in SEDEX deposits, such as the McArthur River (HYC), Mount Isa, and Hilton deposits [85,86]. Py4 crystals with anhedral shapes mostly occur in microfractures within the sediment layers (e.g., dolomitic marble), indicating the compaction during diagenesis. In contrast to Py3 and Py4, Py1, on the basis of its euhedral-to-subhedral pyrite cubes, clearly rules out the replacement model and likely precipitated from a mixture of vent fluid and seawater [87]. Owing to the subhedral and crushed crystals in Py2, the deformation from the late Paleoproterozoic compressional tectonism may have occurred within the Beiwagou deposit. Significantly, the trace element and sulfur isotope compositions in each pyrite type in the Beiwagou deposit suggest that Pb-Zn mineralization likely occurred within the sediments during diagenesis rather than only within the water column.

Mixing the exhalative metalliferous fluids with anoxic seawater caused the crystallization of sulfide particles in the water column along the interface between these two fluids. Sulfide aggregates gravitationally settle at the bottom of the basin, forming typical laminated sulfide textures and euhedral-to-subhedral pyrite cubes (e.g., Py1 and Py2) [88]. After deposition, the compaction and lithification during diagenesis could have induced the precipitated SEDEX-forming fluid to enter the unconsolidated carbonaceous sediments by displacing the less dense sediment pore water, as experimentally modeled by Sangster [89]. Hydrothermal chemical deposition near the sediment-water interface caused sulfate to undergo thermochemical sulfate reduction (TSR), thus turning it into sulfide and producing particulate pyrite and sphalerite. Continued compaction and lithification promoted the loss of permeability and vertical dewatering. Diagenetic fluid transport below the sediment-water interface may have deposited galena, sphalerite, and anhedral pyrite by replacing dolomitic marble during diagenesis.

The Liaodong Peninsula experienced an integrated introversion tectonic process that was initiated at ca. 2.2–2.0 Ga during an intra-continental rifting event and transitioned to an active continental margin at ca. 2.0–1.9 Ga, followed by an arc-continent collision at ca. 1.9 Ga and post-collisional extension at ca. 1.9–1.8 Ga [90]. LA-ICP-MS zircon U-Pb chronology data suggest that the Dashiqiao Formation was formed at 2.17–2.13 Ga while, at ca. 1866 ± 9 Ma, it underwent regional metamorphism [91], indicating that the stratiform Pb-Zn mineralization (SEDEX mineralization) in the Beiwagou ore district occurred during the tectonic setting of intra-continental rifting. The Dashiqiao Formation, as the chief ore-bearing stratum in the Beiwagou Pb-Zn district, is characterized by clastic deposition in the lower section, interbedded clastic deposition and carbonate in the middle section, and carbonate in the upper section, implying a mineralization environment of a transgression sedimentary cycle [35].

7. Conclusions

The Beiwagou sediment-hosted Pb-Zn deposit comprises stratiform orebodies hosted by carbonaceous rocks (e.g., dolomitic marble) of the Paleoproterozoic Gaojiayu and Dashiqiao Formations, similar to those of many SEDEX deposits. Based on the textual and compositional features of pyrite in the Beiwagou deposit, four pyrite generations (Py1, Py2, Py3, and Py4) were identified. Py1 is characterized by high As, Ag, Cd, In, Au, Cu, and Zn concentrations and low Te, Bi, and Mo concentrations, whereas Py2 is characterized by high concentrations of Co and Ni and low concentrations of other trace elements, such as Cu, Zn, Bi, and Te. Py3 was characterized by elevated As, low Co, Ni, In, W, Te, and Tl, and varying Pb concentrations, whereas Py4 was chemically identified by low Ag, Cd, In, Zn, Cu, and Mn and varying W, Co, Ni, Pb, Sb, and As concentrations. Significant correlations

between some elements in each pyrite type suggest substitution mechanisms, such as $(\text{Zn}^{2+} + \text{Cu}^{2+} + \text{Mn}^{2+} + \text{Cd}^{2+}) \leftrightarrow 2\text{Fe}^{2+}$, $\text{Ag}^+ + (\text{Sb})^{3+} \leftrightarrow 2\text{Fe}^{2+}$, and $(\text{Te}^+ + \text{Ag}^+) + \text{Sb}^{3+} \leftrightarrow 2\text{Fe}^{2+}$, and the existence of a negative correlation between Co and Ni implies competition between both elements. The average Co and Ni ratios of 1.38 may indicate pyrite of sedimentary origin, whereas the low Mo content (up to 1.35 ppm) may reflect seawater conditions as widespread oxidizing conditions. Therefore, each pyrite type in the Beiwagou deposit demonstrates the contribution of Paleoproterozoic seawater sulfate to mineralization. The ores have strongly positive $\delta^{34}\text{S}$ values, reflecting thermochemical sulfate reduction at 150 to 200 °C by hydrothermal fluids during diagenesis. Our data suggest that most mineralization events occurred due to the compaction and lithification during diagenesis, which induced sulfate to undergo TSR, loss of permeability, and vertical dewatering.

Supplementary Materials: The following supporting information can be downloaded at: <https://www.mdpi.com/article/10.3390/min13091176/s1>, Table S1. Trace element compositions of each pyrite type in the Beiwagou Pb-Zn deposit.xls.

Author Contributions: Conceptualization, Q.Y. and Z.W.; investigation, Q.Y., Z.W., Q.S. and K.W.; funding acquisition, Z.W. and K.W.; project administration, Z.W. and Q.S.; writing—original draft preparation, Q.Y.; writing—review and editing, Q.Y., Z.W. and Q.S. All authors have read and agreed to the published version of the manuscript.

Funding: This research was financially supported by the National Natural Science Foundation of China (Grants 42102074 and U2244201) and the funding project of Northeast Geological S&T Innovation Center of China Geological Survey (No. QCJJ2022-32).

Data Availability Statement: The experimental data used to support the conclusions of this study are included within the article and supplementary materials.

Acknowledgments: We are grateful to the staff from Beijing Createch Testing Technology Co., Ltd. for their advice and assistance in the experimental analysis. In addition, we wish to thank Xuebing Zhang (Xinjiang University) for providing valuable advice on the manuscript and the anonymous reviewers and editors for their insightful comments.

Conflicts of Interest: The authors declare no conflict of interest.

References

1. Duan, X.X.; Zeng, Q.D.; Wang, Y.B.; Zhou, L.L.; Chen, B. Genesis of the Pb-Zn deposits of the Qingchengzi ore field, eastern Liaoning, China; constraints from carbonate LA-ICPMS trace element analysis and C-O-S-Pb isotopes. *Ore Geol. Rev.* **2017**, *89*, 752–771. [[CrossRef](#)]
2. Li, J.; Cai, W.Y.; Li, B.; Wang, K.Y.; Liu, H.L.; Yassa, K.; Qian, Y.; Lee, G.J.; Yoo, B.C. Paleoproterozoic SEDEX-type stratiform mineralization overprinted by Mesozoic vein-type mineralization in the Qingchengzi Pb-Zn deposit, Northeastern China. *J. Asian Earth Sci.* **2019**, *184*, 104009. [[CrossRef](#)]
3. Liu, J.; Liu, F.X.; Li, S.H.; Lai, C.K. Formation of the Baiyun gold deposit, Liaodong Gold Province, NE China: Constraints from zircon U-Pb age, fluid inclusion, and C-H-O-Pb-He isotopes. *Ore Geol. Rev.* **2019**, *104*, 686–706. [[CrossRef](#)]
4. Li, J.; Wang, K.Y.; Cai, W.Y.; Sun, Q.F.; Liu, H.L.; Fu, L.J.; Qian, Y.; Lai, C.K. Triassic gold-silver metallogenesis in Qingchengzi orefield, North China Craton: Perspective from fluid inclusions, REE and H-O-S-Pb isotope systematics. *Ore Geol. Rev.* **2020**, *121*, 103567. [[CrossRef](#)]
5. Liu, Y.; Wei, J.; Tan, J.; Ulrich, T.; Zhang, D.; Lahaye, Y.; Zhang, X.; Chen, J. Sulfide micro-textures and in-situ compositions from the Wulong gold deposit, northeastern North China Craton: Implication for ore-forming processes. *Ore Geol. Rev.* **2022**, *148*, 105028. [[CrossRef](#)]
6. Ma, Y.B.; Bagas, L.; Xing, S.W.; Zhang, S.T.; Wang, R.J.; Li, N.; Zhang, Z.J.; Zou, Y.F.; Yang, X.Q.; Wang, Y.; et al. Genesis of the stratiform Zhenzigou Pb-Zn deposit in the North China Craton: Rb/Sr and C-O-S-Pb isotope constraints. *Ore Geol. Rev.* **2016**, *79*, 88–104. [[CrossRef](#)]
7. Subias, I.; Fanlo, I.; Yuste, A.; Fernandez-Nieto, C. The Yenefrito Pb-Zn mine (Spanish Central Pyrenees); an example of superimposed metallogenetic events. *Miner. Depos.* **1999**, *34*, 220–223. [[CrossRef](#)]
8. Magnall, J.M.; Gleeson, S.A.; Paradis, S. A new subseafloor replacement model for the macmillan pass clastic-dominant Zn-Pb ± Ba deposits (Yukon, Canada). *Econ. Geol.* **2020**, *115*, 953–959. [[CrossRef](#)]
9. Slack, J.F.; Kelley, K.D.; Anderson, V.M.; Clark, J.L.; Ayuso, R.A. Multistage hydrothermal silicification and Fe-Tl-As-Sb-Ge-REE enrichment in the Red Dog Zn-Pb-Ag district, northern Alaska: Geochemistry, origin, and exploration applications. *Econ. Geol.* **2004**, *99*, 1481–1508. [[CrossRef](#)]

10. Shu, Q.; Chang, Z.; Mavrogenes, J. Fluid compositions reveal fluid nature, metal deposition mechanisms, and mineralization potential: An example at the Haobugao Zn-Pb skarn, China. *Geology* **2021**, *49*, 473–477. [[CrossRef](#)]
11. Shu, Q.; Chang, Z.; Hammerli, J.; Lai, Y.; Huizenga, J.-M. Composition and evolution of fluids forming the Baiyinnuo'er skarn Zn-Pb deposit, northeastern China: Insights from laser ablation ICP-MS study of fluid inclusions. *Econ. Geol.* **2017**, *112*, 1441–1460. [[CrossRef](#)]
12. Liu, Q.; Mei, Y.; Etschmann, B.; Glenn, M.; MacRae, C.M.; Spinks, S.C.; Ryan, C.G.; Brugger, J.; Paterson, D.J. Germanium speciation in experimental and natural sphalerite: Implications for critical metal enrichment in hydrothermal Zn-Pb ores. *Geochim. Cosmochim. Acta* **2023**, *342*, 198–214. [[CrossRef](#)]
13. Esra, Ü.Ç.; Ahmet, G.; Chris, H. Genesis of Tertiary Akçaklı vein-type Pb-Zn-Cu mineralisation (Central Anatolia, Turkey): Evidence from fluid inclusion and O, H, S, Pb-isotope compositions. *J. Afr. Earth Sci.* **2023**, *205*, 105008.
14. Wang, K.Y.; Zhao, Y.M.; Cao, X.L. *The Proterozoic Type Lead-Zinc Deposits in Northern Border of North China Platform*; Geological Publishing House: Beijing, China, 1994; p. 190. (In Chinese)
15. Jiang, S.Y. Pb-Isotope Composition at Qingchengzi Lead-Zinc Deposit and Its Geological Application. *J. Peking Univ. (Nat. Sci.)* **1987**, *23*, 112–119. (In Chinese with English Abstract).
16. Ding, T.P.; Jiang, S.Y.; Wan, D.F.; Li, J.C.; Song, B.; Zhao, D.M. *Stable Isotope Studies on the Proterozoic Pb-Zn Mineral Belt of Northern China*; Beijing Publishing House of Science and Technology: Beijing, China, 1992; pp. 36–60. (In Chinese)
17. Leach, D.L.; Marsh, E.; Emsbo, P.; Rombach, C.S.; Kelley, K.D.; Anthony, M. Nature of Hydrothermal Fluids at the Shale-Hosted Red Dog Zn-Pb-Ag Deposits, Brooks Range, Alaska. *Econ. Geol.* **2004**, *99*, 1449–1480. [[CrossRef](#)]
18. Leach, D.L.; Bradley, D.C.; Huston, D.; Pisarevsky, S.A.; Taylor, R.D.; Gardoll, S.J. Sediment-Hosted Lead-Zinc Deposits in Earth History. *Econ. Geol.* **2010**, *105*, 593–625. [[CrossRef](#)]
19. Gadd, M.G.; Layton-Matthews, D.; Peter, J.M.; Paradis, S.J. The world-class Howard's Pass SEDEX Zn-Pb district, Selwyn Basin, Yukon; Part I, trace element compositions of pyrite record input of hydrothermal, diagenetic, and metamorphic fluids to mineralization. *Miner. Depos.* **2016**, *51*, 319–342. [[CrossRef](#)]
20. Huston, D.L.; Sie, S.H.; Suter, G.F.; Cooke, D.R.; Both, R.A. Trace elements in sulfide minerals from eastern Australian volcanic-hosted massive sulfide deposits: Part I. Proton microprobe analyses of pyrite, chalcopyrite, and sphalerite, and Part II. Selenium levels in pyrite: Comparison with $\delta^{34}\text{S}$ values and implications for the source of sulfur in volcanogenic hydrothermal systems. *Econ. Geol.* **1995**, *90*, 1167–1196.
21. Deditius, A.P.; Utsunomiya, S.; Reich, M.; Kesler, S.E.; Ewing, R.C.; Hough, R.; Walshe, J. Trace metal nanoparticles in pyrite. *Ore Geol. Rev.* **2011**, *42*, 32–46. [[CrossRef](#)]
22. Large, R.R.; Danyushevsky, L.; Hollit, C.; Maslennikov, V.; Meffre, S.; Gilbert, S.; Bull, S.; Scott, R.; Emsbo, P.; Thomas, H.; et al. Gold and Trace Element Zonation in Pyrite Using a Laser Imaging Technique: Implications for the Timing of Gold in Orogenic and Carlin-style Sediment-Hosted Deposits. *Econ. Geol.* **2009**, *104*, 635–668. [[CrossRef](#)]
23. Reich, M.; Deditius, A.; Chryssoulis, S.; Li, J.W.; Ma, C.Q.; Parada, M.A.; Barra, F.; Mittermayr, F. Pyrite as a record of hydrothermal fluid evolution in a porphyry copper system: A SIMS/EMPA trace element study. *Geochim. Cosmochim. Acta* **2013**, *104*, 42–62. [[CrossRef](#)]
24. Gregory, D.; Meffre, S.; Large, R. Comparison of metal enrichment in pyrite framboids from a metal-enriched and metal-poor estuary. *Am. Mineral.* **2014**, *99*, 633–644. [[CrossRef](#)]
25. Doyle, M.G.; Allen, R.L. Subsea-floor replacement in volcanic-hosted massive sulfide deposits. *Ore Geol. Rev.* **2003**, *23*, 183–222. [[CrossRef](#)]
26. Rona, P.A.; Bostrom, K.; Laubier, L.; Smith, K.L. Hydrothermal mineralization at seafloor spreading centers. *Earth-Sci. Rev.* **1984**, *20*, 1–104. [[CrossRef](#)]
27. Chen, F.; Deng, J.; Wang, Q.; Huizenga, J.M.; Li, G.; Gu, Y. LA-ICP-MS trace element analysis of magnetite and pyrite from the Hetaoping Fe-Zn-Pb skarn deposit in Baoshan block, SW China: Implications for ore-forming processes. *Ore Geol. Rev.* **2020**, *117*, 103309. [[CrossRef](#)]
28. Wagner, T.; Klemd, R.; Wenzel, T.; Mattsson, B. Gold upgrading in metamorphosed massive sulfide ore deposits: Direct evidence from laser-ablation-inductively coupled plasma-mass spectrometry analysis of invisible gold. *Geology* **2007**, *35*, 775–778. [[CrossRef](#)]
29. Genna, D.; Gaboury, D. Deciphering the Hydrothermal Evolution of a VMS System by LA-ICP-MS Using Trace Elements in Pyrite: An Example from the Bracemac-McLeod Deposits, Abitibi, Canada, and Implications for Exploration. *Econ. Geol.* **2015**, *110*, 2087–2108. [[CrossRef](#)]
30. Hazarika, P.; Mishra, B.; Saravanan Chinnasamy, S.; Bernhardt, H.J. Multi-stage growth and invisible gold distribution in pyrite from the Kundarkocha sediment-hosted gold deposit, eastern India. *Ore Geol. Rev.* **2013**, *55*, 134–145. [[CrossRef](#)]
31. Mason, P.R.D.; Košler, J.; de Hoog, J.C.M.; Sylvester, P.J.; Meffan-Main, S. In situ determination of sulfur isotopes in sulfur-rich materials by laser ablation-multiple collector-inductively coupled plasma-mass spectrometry (LA-MC-ICP-MS). *J. Anal. At. Spectrom.* **2006**, *21*, 177–186. [[CrossRef](#)]
32. Ulrich, T.; Long, D.G.F.; Kamber, B.S.; Whitehouse, M.J. In situ trace element and sulfur isotope analysis of pyrite in a Paleoproterozoic gold placer deposit, Pardo and Clement Townships, Ontario, Canada. *Econ. Geol.* **2011**, *106*, 667–686. [[CrossRef](#)]

33. Gadd, M.G.; Layton-Matthews, D.; Peter, J.M.; Paradis, S.; Jonasson, I.R. The world-class Howard's Pass SEDEX Zn-Pb district, Selwyn Basin, Yukon. Part II: The roles of thermochemical and bacterial sulfate reduction in metal fixation. *Miner. Depos.* **2017**, *52*, 405–419. [[CrossRef](#)]
34. Qiu, W.J.; Zhou, M.F.; Li, X.C.; Williams-Jones, A.E.; Yuan, H.L. The Genesis of the Giant Dajiangping SEDEX-Type Pyrite Deposit, South China. *Econ. Geol.* **2018**, *113*, 1419–1446. [[CrossRef](#)]
35. Gao, C.Y.; Wang, J.G.; Zhao, Y. *Liaoning Xiuyan Manchu Autonomous County North Tile Pb-Zn Deposit Geological Report Detailed Survey*; National Geological Library: Beijing, China, 1990; pp. 1–160. (In Chinese)
36. Jiang, Y.; Liu, X.L. The Discovery of Epiboulangerite and Its Relation with Gold mineralization in Beiwagou Lead-Zinc mine. *Miner. Resour. Geol.* **1998**, *5*, 26–30. (In Chinese)
37. Song, B.; Nutman, A.P.; Liu, D.Y.; Wu, J. 3800 to 2500 Ma crustal evolution in the Anshan area of Liaoning Province, Northeastern China. *Precambr. Res.* **1996**, *78*, 79–94. [[CrossRef](#)]
38. Zhang, Q.S.; Yang, Z.S.; Wang, Y.J. *Early Crust and Mineral Deposits of Liaodong Peninsula*; Geological Publishing House: Beijing, China, 1988. (In Chinese)
39. Zhang, P. Metallogenetic Characteristics, Ore Genesis, Diagenesis and Metallogenetic Geodynamic Process of Precious and Non Ferrous Metals Ore Deposits in Southeast Liaoning Province. Ph.D. Thesis, Jilin University, Changchun, China, 2018. (In Chinese with English Abstract).
40. Li, H.; Zhang, Z.; Li, L.; Zhang, Z.; Chen, J.; Yao, T. Types and general characteristics of the BIF-related iron deposits in China. *Ore Geol. Rev.* **2014**, *57*, 264–287. [[CrossRef](#)]
41. Tian, F.; Wang, K.Y.; Liang, Y.H.; Li, S.H.; Dong, G.H. Characteristics of Hydrothermal Superimposed Mineralization and Source of Ore-Forming Fluids in the Dahenglu Co-Cu Deposit. *Northwest. Geol.* **2017**, *50*, 167–177. (In Chinese)
42. Yan, X.L.; Chen, B. Chemical and boron isotopic compositions of tourmaline from the Paleoproterozoic Houxianyu borate deposit, NE China: Implications for the origin of borate deposit. *J. Asian Earth Sci.* **2014**, *94*, 252–266. [[CrossRef](#)]
43. Li, J. Metallogenesis of Lead-Zinc-Gold-Silver in the Qingchengzi Orefield, Liaoning Province. Ph.D. Thesis, Jilin University, Changchun, China, 2020. (In Chinese with English Abstract).
44. Luo, Y.X.; Zhu, J.R.; Wang, Y.K. A preliminary study on the genesis of the Dahiqiao sparry magnesite deposit in the light of some geological feature. *Miner. Depos.* **1989**, *1*, 71–84, (In Chinese with English Abstract).
45. Meng, E.; Wang, C.Y.; Liu, C.H.; Shi, J.R.; Li, Y.G. Geochronology and Petrogenesis and Constraints on Regional Tectonic Evolution of the Meta-Volcanic Rocks in Southeastern Liaodong Peninsula. *J. Jilin Univ. (Earth Sci. Ed.)* **2017**, *47*, 1589–1619, (In Chinese with English Abstract).
46. Yang, C.W.; Zhang, J.; Zhao, L.F.; Zhang, C.; Yang, H.X.; Lu, T.J.; Liu, J.L. Detrital zircon constraints on tectonic evolution of the Liaodong Paleoproterozoic orogenic belt, North China Craton. *Precambr. Res.* **2021**, *362*, 106152. [[CrossRef](#)]
47. Yang, J.H.; Wu, F.Y.; Liu, X.M.; Xie, L.W.; Yang, Y.H. Petrogenesis and geologic significance of the Jurassic Xiaoheishan pluton in the Liaodong Peninsula, East China: In-situ zircon U-Pb dating and Hf isotope analysis. *Bull. Mineral. Petrol. Geochem.* **2007**, *26*, 197–211, (In Chinese with English Abstract).
48. Yu, G.; Chen, J.F.; Xue, C.J.; Chen, Y.C.; Chen, F.K.; Du, X.Y. Geochronological framework and Pb, Sr isotope geochemistry of the Qingchengzi Pb-Zn-Ag-Au orefield, Northeastern China. *Ore Geol. Rev.* **2009**, *35*, 367–382. [[CrossRef](#)]
49. Duan, X.X.; Zeng, Q.D.; Yang, J.H.; Liu, J.M.; Wang, Y.B.; Zhou, L.L. Geochronology, geochemistry and Hf isotope of Late Triassic magmatic rocks of Qingchengzi district in Liaodong peninsula, Northeast China. *J. Asian Earth Sci.* **2014**, *91*, 107–124. [[CrossRef](#)]
50. Zhou, G.C.; Wang, Y.W.; Li, D.D.; Shi, Y.; Xie, H.J. LA-ICP-MS Zircon U-Pb Dating of Dykes from the Baiyun Gold Deposit in Eastern Liaoning. *Bull. Mineral. Petrol. Geochem.* **2017**, *36*, 620–627, (In Chinese with English Abstract).
51. Wu, F.Y.; Yang, J.H.; Liu, X.M. Geochronological Framework of the Mesozoic Granitic Magmatism in the Liaodong Peninsula, Northeast China. *Geol. J. China Univ.* **2005**, *11*, 305–317, (In Chinese with English Abstract).
52. Yu, B.; Zeng, Q.D.; Frimmel, H.E.; Qiu, H.C.; Li, Q.L.; Yang, J.H.; Wang, Y.B.; Zhou, L.L.; Chen, P.W.; Li, J.P. The 127 Ma gold mineralization in the Wulong deposit, Liaodong Peninsula, China: Constraints from molybdenite Re-Os, monazite U-Th-Pb, and zircon U-Pb geochronology. *Ore Geol. Rev.* **2020**, *121*, 103542. [[CrossRef](#)]
53. Sun, G.T.; Zeng, Q.D.; Zhou, J.X.; Zhou, L.L.; Chen, P.W. Genesis of the Xinling vein-type Ag-Pb-Zn deposit, Liaodong Peninsula, China: Evidence from texture, composition and in situ S-Pb isotopes. *Ore Geol. Rev.* **2021**, *133*, 104120. [[CrossRef](#)]
54. Li, S.Z.; Zhao, G.C.; Sun, M.; Wu, F.Y.; Liu, J.Z.; Hao, D.F.; Han, Z.Z.; Luo, Y. Mesozoic, not paleoproterozoic SHRIMP U-Pb Zircon Ages of Two Liaoji Granites, Eastern Block, North China Craton. *Int. Geol. Rev.* **2004**, *46*, 162–176. [[CrossRef](#)]
55. Chang, R.H.; Liu, Y.J.; Li, W.M.; Gu, D.X. Deformation and rheological properties of Dashiqiao Formation of Liaohe Group in Hupiyu area, eastern Liaoning Province. *Geol. J.* **2019**, *54*, 804–818. [[CrossRef](#)]
56. Wang, F.; Liu, F.L.; Schertl, H.P.; Wang, X.; Liu, P.H.; Tian, Z.H. Detrital zircon U-Pb geochronology and Hf isotopes of the Liaohe Group, Jiao-Liao-Ji Belt: Implications for the Paleoproterozoic tectonic evolution. *Precambr. Res.* **2020**, *340*, 105633. [[CrossRef](#)]
57. Liu, Y.S.; Hu, Z.C.; Gao, S.; Günther, D.; Xu, J.; Gao, C.G.; Chen, H.H. In-situ Analysis of Major and Trace Elements of Anhydrous Minerals by LA-ICP-MS without Applying an Internal Standard. *Chem. Geol.* **2008**, *257*, 34–43. [[CrossRef](#)]
58. Pearce, N.J.G.; Perkins, W.T.; Westgate, J.A.; Gorton, M.P.; Chenery, S.P. A Compilation of new and published major and trace element data for NIST SRM 610 and NIST SRM 612 glass reference materials. *Geostand. Geoanal. Res.* **1997**, *21*, 115–144. [[CrossRef](#)]

59. Price, B.J. Minor Elements in Pyrites from the Smithers Map Area, B.C. and Exploration Applications of Minor Element Studies. Master’s Thesis, The University of British Columbia, Vancouver, BC, Canada, 1972.
60. Tribouillard, N.; Algeo, T.J.; Lyons, T.; Riboulleau, A. Trace metals as paleoredox and paleoproductivity proxies: An update. *Chem. Geol.* **2006**, *232*, 12–32. [[CrossRef](#)]
61. Thomas, H.V.; Large, R.R.; Bull, S.W.; Maslennikov, V.; Berry, R.F.; Fraser, R.; Froud, S.; Moye, R. Pyrite and Pyrrhotite Textures and Composition in Sediments, Laminated Quartz Veins, and Reefs at Bendigo Gold Mine, Australia: Insights for Ore Genesis. *Econ. Geol.* **2011**, *106*, 1–31. [[CrossRef](#)]
62. Meng, Y.M.; Hu, R.Z.; Huang, X.W.; Gao, J.F.; Sasseville, C. The origin of the carbonate-hosted Huize Zn–Pb–Ag deposit, Yunnan province, SW China: Constraints from the trace element and sulfur isotopic compositions of pyrite. *Mineral. Petrol.* **2019**, *113*, 369–391. [[CrossRef](#)]
63. Algeo, T.J.; Lyons, T.W. Mo-total organic carbon covariation in modern anoxic marine environments: Implications for analysis of paleoredox and paleohydrographic conditions. *Paleoceanography* **2006**, *21*, 1–23. [[CrossRef](#)]
64. Reich, M.; Kesler, S.E.; Utsunomiya, S.; Palenik, C.S.; Chrysoulis, S.L.; Ewing, R.C. Solubility of gold in arsenian pyrite. *Geochim. Cosmochim. Acta* **2005**, *69*, 2781–2796. [[CrossRef](#)]
65. Morse, J.W.; Luther, G.W. Chemical influences on trace metal-sulfide interactions in anoxic sediments. *Geochim. Cosmochim. Acta* **1999**, *63*, 3373–3378. [[CrossRef](#)]
66. Maslennikov, V.V.; Maslennikova, S.P.; Large, R.R.; Danyushevsky, L.V. Study of Trace Element Zonation in Vent Chimneys from the Silurian Yaman-Kasy Volcanic-Hosted Massive Sulfide deposit (Southern Urals, Russia) Using Laser Ablation-Inductively Coupled Plasma Mass Spectrometry (LA-ICPMS). *Econ. Geol.* **2009**, *104*, 1111–1141. [[CrossRef](#)]
67. Grant, H.L.J.; Hannington, M.D.; Petersen, S.; Frische, M.; Fuchs, S.H. Constraints on the behavior of trace elements in the actively-forming TAG deposit, Mid-Atlantic Ridge, based on LA-ICP-MS analyses of pyrite. *Chem. Geol.* **2018**, *498*, 45–71. [[CrossRef](#)]
68. Rollinson, H.R. A terrane interpretation of the Archaean Limpopo Belt. *Geol. Mag.* **1993**, *130*, 755–765. [[CrossRef](#)]
69. Leach, D.L.; Sangster, D.F.; Kelley, K.D.; Large, R.R.; Garven, G.; Allen, C.R.; Gutzmer, J.; Walters, S.G. Sediment-hosted lead-zinc deposits: A global perspective. In *Economic Geology 100th Anniversary Volume*; Society of Economic Geologists: Littleton, CO, USA, 2005; pp. 561–607.
70. Ohmoto, H. Systematics of Sulfur and Carbon isotopes in Hydrothermal Ore Deposits. *Econ. Geol.* **1972**, *67*, 551–578. [[CrossRef](#)]
71. Cooke, D.R.; Bull, S.W.; Large, R.R.; McGoldrick, P.J. The Importance of Oxidized Brines for the Formation of Australian Proterozoic stratiform Sediment-Hosted Pb-Zn (SEDEX) Deposits. *Econ. Geol.* **2000**, *95*, 1–18. [[CrossRef](#)]
72. Paiste, K.; Lepland, A.; Zerkle, A.L.; Kirsimäe, K.; Kreitsmann, T.; Mänd, K.; Romashkin, A.E.; Rychanchik, D.V.; Prave, A.R. Identifying global vs. basinal controls on Paleoproterozoic organic carbon and sulfur isotope records. *Earth-Sci. Rev.* **2020**, *207*, 103230. [[CrossRef](#)]
73. Scott, C.; Wing, B.A.; Bekker, A.; Planavsky, N.J.; Medvedev, P.; Bates, S.M.; Yun, M.; Lyons, T.W. Pyrite multiple-sulfur isotope evidence for rapid expansion and contraction of the early Paleoproterozoic seawater sulfate reservoir. *Earth Planet. Sci. Lett.* **2014**, *389*, 95–104. [[CrossRef](#)]
74. Williford, K.H.; Van Kranendonk, M.J.; Ushikubo, T.; Kozdon, R.; Valley, J.W. Constraining atmospheric oxygen and seawater sulfate concentrations during Paleoproterozoic glaciation: In situ sulfur three-isotope microanalysis of pyrite from the Turee Creek Group, Western Australia. *Geochim. Cosmochim. Acta* **2011**, *75*, 5686–5705. [[CrossRef](#)]
75. Froelich, P.N.; Klinkhammer, G.P.; Bender, M.L.; Luedtke, N.A.; Heath, G.R.; Cullen, D.; Dauphin, P.; Hammond, D.; Hartman, B.; Maynard, V. Early oxidation of organic matter in pelagic sediments of the eastern equatorial Atlantic: Suboxic diagenesis. *Geochim. Cosmochim. Acta* **1979**, *43*, 1075–1090. [[CrossRef](#)]
76. Machel, H.G. Bacterial and thermochemical sulfate reduction in diagenetic settings—Old and new insights. *Sediment. Geol.* **2001**, *140*, 143–175. [[CrossRef](#)]
77. Leavitt, W.D.; Halevy, I.; Bradley, A.S.; Johnston, D.T. Influence of sulfate reduction rates on the Phanerozoic sulfur isotope record. *Proc. Natl. Acad. Sci. USA* **2013**, *110*, 11244–11249. [[CrossRef](#)]
78. Anderson, I.K.; Ashton, J.H.; Boyce, A.J.; Fallick, A.E.; Russell, M.J. Ore depositional processes in the Navan Zn-Pb deposit, Ireland. *Econ. Geol.* **1998**, *93*, 535–563. [[CrossRef](#)]
79. Martin, A.J.; McDonald, I.; Jamieson, J.W.; Jenkin, G.R.T.; McFall, K.A.; Piercy, G.; MacLeod, C.J.; Layne, G.D. Mineral-scale variation in the trace metal and sulfur isotope composition of pyrite: Implications for metal and sulfur sources in mafic VMS deposits. *Miner. Depos.* **2022**, *57*, 911–933. [[CrossRef](#)]
80. Machel, H.G.; Krouse, H.R.; Sassen, R. Products and distinguishing criteria of bacterial and thermochemical sulfate reduction. *Appl. Geochem.* **1995**, *10*, 373–389. [[CrossRef](#)]
81. Rivai, T.A.; Yonezu, K.; Tindell, T.; Boyce, A.J.; Sanematsu, K.; Satori, S.; Watanabe, K. The Dairi SEDEX Zn + Pb + Ag deposit (North Sumatra, Indonesia): Insights from mineralogy and sulfur isotope systematics. *Ore Geol. Rev.* **2020**, *122*, 103510. [[CrossRef](#)]
82. Ireland, T.; Large, R.R.; McGoldrick, P.; Blake, M. Spatial Distribution Patterns of Sulfur Isotopes, Nodular Carbonate, and Ore Textures in the McArthur River (HYC) Zn-Pb-Ag Deposit, Northern Territory, Australia. *Econ. Geol.* **2004**, *99*, 1687–1709. [[CrossRef](#)]

83. Magnall, J.M.; Gleeson, S.A.; Stern, R.A.; Newton, R.J.; Poulton, S.W.; Paradis, S. Open system sulphate reduction in a diagenetic environment—Isotopic analysis of barite ($\delta^{34}\text{S}$ and $\delta^{18}\text{O}$) and pyrite ($\delta^{34}\text{S}$) from the Tom and Jason Late Devonian Zn-Pb-Ba deposits, Selwyn Basin, Canada. *Geochim. Cosmochim. Acta* **2016**, *180*, 146–163. [[CrossRef](#)]
84. Large, R.R.; Halpin, J.A.; Danyushevsky, L.V.; Maslennikov, V.V.; Bull, S.W.; Long, J.A.; Gregory, D.D.; Lounejeva, E.; Lyons, T.W.; Sack, P.J.; et al. Trace element content of sedimentary pyrite as a new proxy for deep-time ocean–atmosphere evolution. *Earth Planet. Sci. Lett.* **2014**, *389*, 209–220. [[CrossRef](#)]
85. Perkins, W.G.; Bell, T.H. Stratiform Replacement Lead-Zinc Deposits: A Comparison between Mount Isa, Hilton, and McArthur River. *Econ. Geol.* **1998**, *93*, 1190–1212. [[CrossRef](#)]
86. Eldridge, C.S.; Williams, N.; Walshe, J.L. Sulfur Isotope Variability in Sediment-Hosted Massive Sulfide Deposits as Determined Using the Ion Microprobe SHRIMP: II. A Study of the H.Y.C Deposit at McArthur River, Northern Territory, Australia. *Econ. Geol.* **1993**, *88*, 1–26. [[CrossRef](#)]
87. Feel, R.A.; Geiselman, T.L.; Baker, E.T.; Massoth, G.J.; Hammond, S.R. Distribution and composition of hydrothermal plume particles from the ASHES Vent Field at Axial Volcano, Juan de Fuca Ridge. *J. Geophys. Res.* **1990**, *95*, 12855–12873. [[CrossRef](#)]
88. Large, R.R.; Bull, S.W.; McGoldrick, P.J.; Walters, S.; Derrick, G.M.; Carr, G.R. Stratiform and strata-bound Zn-Pb-Ag deposits in Proterozoic sedimentary basins, northern Australia. In *Economic Geology 100th Anniversary Volume*; Society of Economic Geologists: Littleton, CO, USA, 2005; pp. 931–963.
89. Sangster, D.F. The role of dense brines in the formation of vent-distal sedimentary-exhalative (SEDEX) lead-zinc deposits: Field and laboratory evidence. *Miner. Depos.* **2002**, *37*, 149–157. [[CrossRef](#)]
90. Liu, J.; Zhang, J.; Liu, Z.H.; Yin, C.Q.; Zhao, C.; Li, Z.; Yang, Z.J.; Dou, S.Y. Geochemical and geochronological study on the Paleoproterozoic rock assemblage of the Xiuyan region: New constraints on an integrated rift-and-collision tectonic process involving the evolution of the Jiao-Liao-Ji Belt, North China Craton. *Precambr. Res.* **2018**, *310*, 179–197. [[CrossRef](#)]
91. Dong, Y.; Bi, J.H.; Xing, D.H.; Ge, W.C.; Jing, Y. Geochronology and geochemistry of Liaohe Group and Liaoji granitoid in the Jiao-Liao-Ji Belt, North China Craton: Implications for petrogenesis and tectonic evolution. *Precambr. Res.* **2019**, *332*, 105399. [[CrossRef](#)]

Disclaimer/Publisher’s Note: The statements, opinions and data contained in all publications are solely those of the individual author(s) and contributor(s) and not of MDPI and/or the editor(s). MDPI and/or the editor(s) disclaim responsibility for any injury to people or property resulting from any ideas, methods, instructions or products referred to in the content.